IOPscience iopscience.iop.org

Home Search Collections Journals About Contact us My IOPscience

Transient stimulated emission from multi-split-gated graphene structure

This content has been downloaded from IOPscience. Please scroll down to see the full text.

2014 J. Phys. D: Appl. Phys. 47 055103

(http://iopscience.iop.org/0022-3727/47/5/055103)

View the table of contents for this issue, or go to the journal homepage for more

Download details:

IP Address: 130.34.208.207
This content was downloaded on 07/01/2014 at 00:27

Please note that terms and conditions apply.

IOP Publishing
Journal of Physics D: Applied Physics
J. Phys. D: Appl. Phys. **47** (2014) 055103 (8pp)
doi:10.1088/0022-3727/47/5/055103

Transient stimulated emission from multi-split-gated graphene structure

A Satou[1], F T Vasko[1,3], T Otsuji[1] and V V Mitin[2]

[1] Research Institute of Electrical Communication, Tohoku University, Sendai 980-8577, Japan
[2] Department of Electrical Engineering, University at Buffalo, Buffalo, NY 1460-1920, USA

E-mail: a-satou@riec.tohoku.ac.jp

Received 25 July 2013, revised 17 November 2013
Accepted for publication 29 November 2013
Published 31 December 2013

Abstract
Mechanism of transient population inversion in graphene with multi-split (interdigitated) top-gate and grounded back gate is suggested and examined for the mid-infrared spectral region. Efficient stimulated emission after fast lateral spreading of carriers due to drift–diffusion processes is found for the case of a slow electron–hole recombination in the passive region. We show that with the large gate-to-graphene distance, the drift process always precedes the diffusion process, due to the ineffective screening of the inplane electric field by the gates. Conditions for lasing with a gain above 100 cm^{-1} are found for cases of single- and multi-layer graphene placed in the waveguide formed by the top and back gates. Both the waveguide losses and temperature effects are analysed.

Keywords: mid-infrared laser, graphene, population inversion

(Some figures may appear in colour only in the online journal)

1. Introduction

Conventional scheme of semiconductor laser [1] is based on population inversion between electron states in conduction and valence bands, so that the emission wavelength is determined by the bandgap of the material used (typically, lasing takes place in a spectral region from near-IR to far-UV). Lasers for mid-infrared (mid-IR) and THz regions were realized based on the tunnel-coupled heterostructures (quantum cascade scheme [2]) or on the *p*-type bulk materials with the degenerate valence bands [3]. Active studies of graphene, which is a two-dimensional gapless semiconductor with unusual physical characteristics [4], involve both theoretical investigation of the stimulated emission regime under steady-state or ultrafast pumping [5, 6] and experimental attempts—approaches for realization of lasing. Recently, the transformation of the ultrafast optical pumping into THz or near-IR radiation was reported, see [7–9]. Due to the emission of optical phonons after the ultrafast pumping [7], these approaches should lose an efficiency with increasing pulse duration. In order to avoid the suppression of stimulated emission, one needs a pumping scheme which permits creation of dense electron–hole plasma without involvement of the high-energy states when the optical-phonon emission becomes essential. Thus, investigation of alternative pumping mechanisms for realization of population inversion in electron–hole plasma of graphene is timely now.

In this paper, we suggest a new pumping scheme for a graphene layer modulated by spatio-temporally varied voltages applied through multi-split gates (MSGs), see the structure in figure 1(*a*). Such structures have been studied for THz plasmonic devices [10], for excellent coupling between two-dimensional plasmons and THz waves. For our purpose, the MSG structure enables us to induce spatially separated electrons and holes in the graphene layer by bias voltages at the initial time and then to induce the interband population inversion through the entire layer by lateral drift and diffusion processes. An initial periodical modulation of electron and hole concentrations shown in figure 1(*b*) takes place at $t \leqslant 0$ under bipolar voltages $\pm V_g$ applied through the top gates of the MSG structure. Temporal evolution of the initial charge distributions due to lateral spreading of carriers after abrupt switch-off voltages $\pm V_g$ at $t \geqslant 0$ is shown in the middle panel of figure 1(*b*). If recombination processes are negligible, in-plane spreading of electrons and holes drifted by the electric field created by themselves takes place with a timescale t_D,

[3] Present address: QK Applications, San Francisco, CA 94033, USA.

 © 2014 IOP Publishing Ltd Printed in the UK

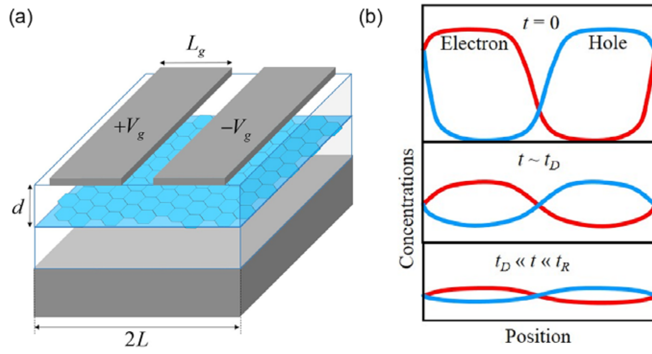

Figure 1. (*a*) Multi-split-gated structure under initial biases $+V_g$ and $-V_g$ with a grounded back gate at the bottom. (*b*) Transient evolution of charge concentrations after switching off the voltages $\pm V_g$ at $t = 0$ when lateral drift and diffusion processes take place during time intervals $t \sim t_D$ and $t_D \ll t \ll t_R$, where t_D and t_R are the characteristic timescales of the drift–diffusion and recombination processes, respectively.

followed by their diffusion within time $t_D \ll t \ll t_R$, where t_R is the characteristic time for non-radiative recombination, without changing the total electron and hole concentrations which are determined by the initial conditions at $t \leqslant 0$. The MSG structure also works as a waveguide where the multi-split top and back gates define the vertical confinement and waves propagate along the waveguide. By having many periods, the waveguide can work in the mid-IR region, in which the wavelength is several times larger than one period ($\sim 5\,\mu$m).

Under a typical disorder level, the drift–diffusive hydrodynamic equations describe regime of spreading at $t > 0$, when the initial distributions transform into homogeneous quasi-Fermi distributions of electrons and holes. If transient stimulated emission due to direct interband transition in the spectral region $\hbar\omega \leqslant 2\varepsilon_F$ takes place during timescales less than or comparable to the characteristic time t_D in the passive region (at energies less than a half of the optical-phonon energy), an effective regime for the transient stimulated emission is accomplished.

The paper is organized as follows. In the next section we calculate the distributions of carriers in the biased structure under consideration. In section 3, we analyse the process of lateral drift and diffusion of carriers after the bias voltages are abruptly switched-off. The transient lasing regime is considered in section 4. The last section includes the list of approximations used and conclusions. In the appendix we evaluate the hydrodynamic equations describing a temporal evolution of non-uniform electron–hole plasma.

2. Initial electron and hole distributions

We start from consideration of the initial distribution of electron and hole concentrations under the biases $\pm V_g$ applied through the multi-split top gates separated by the distance d from graphene placed at $z = 0$ over the substrate with the grounded bottom gate at $z = -d$. The two-dimensional Poisson equation

$$\frac{\partial^2\varphi}{\partial x^2} + \frac{\partial^2\varphi}{\partial z^2} = 0, \qquad |z| < d, \quad |x| < L \tag{1}$$

should be supplied by periodic boundary conditions along the structure (x-direction, here $2L$ is the length of the two-strip element with $+V_g$ and $-V_g$ voltages), boundary conditions at the top gates and bottom gate, $\varphi|_{|x\pm L/2|<L_g/2, z=d} = \pm V_g$ and $\varphi|_{z=-d} = 0$, and boundary conditions far from the structure, $(\partial\varphi/\partial z)_{x,z\to\infty} = 0$. Boundary conditions at the graphene layer are given by the continuity requirement $\varphi|_{z=-0}^{z=+0} = 0$ and the Gauss theorem:

$$\left.\frac{\partial\varphi}{\partial z}\right|_{z=-0}^{z=+0} = -\frac{4\pi}{\epsilon}\rho. \tag{2}$$

Here ϵ is the static dielectric constant, which is the same for the layers under and above the graphene layer, and $\rho = \rho_e + \rho_h$ is the total charge density in the graphene layer, where ρ_e and ρ_h are the electron and hole charge densities, respectively.

Initial distributions of the potential and the charge densities can be found by solving equation (1) self-consistently with the following relation between the charge densities and the potential in the graphene layer, $\varphi|_{z=0}$:

$$\rho_r = s_r \frac{4e}{2\pi\hbar^2}\int_0^\infty \mathrm{d}p\, p f_F(p, -s_r e\varphi|_{z=0}, T), \tag{3}$$

where $s_e = -1$ and $s_h = +1$, T is the carrier temperature, and $f_F(p, E, T) = \{1 + \exp[(vp - E)/T]\}^{-1}$ is the quasi-Fermi distribution with the carrier velocity $v = 10^8$ cm s^{-1}.

The charge densities and potential would be obtained from equations (1) and (3) analytically as $|\rho_r| = \rho_s = \epsilon V_g/4\pi d = C_s V_g$ and $\varphi = \varphi_s = \sqrt{\pi\hbar^2 v^2 C_s V_g/2e^3}$, in the case when the parallel-plate model could be applicable, the temperature would be zero, and the quantum capacitance of graphene could be ignored. However, the parallel-plate model is not applicable in our case, due to the limitation of the vertical dimension d that determines the operating frequency of the waveguide structure and the magnitude of gate voltages in order to have population inversion up to that frequency. Intending waveguide structures operating at mid-IR wavelengths, in the discussion below we shall set the structural parameters as $d = 1.5$–$4\,\mu$m, $L = 1.5$–$6\,\mu$m, $L_g = 0.5$–$2\,\mu$m, and $\epsilon = 4$ (SiO_2) and with thickness of the gates fixed to 10 nm. However, it should be mentioned that SiO_2 has sharp absorption peaks at 9 and 21 μm [11]. Therefore, we shall focus on $\lambda = 12\,\mu$m, 15 μm and 30 μm (corresponding to $f = 25$ THz, 20 THz and 10 THz, respectively). In general, either adapting non-polar waveguide materials or avoiding absorption peaks in polar materials is preferable to avoid the dielectric loss in the THz/mid-IR region.

Figure 2 shows the normalized potential distribution, φ/V_g, with $d = 1.5\,\mu$m, $L = 2\,\mu$m and $L_g = 0.5\,\mu$m at $T = 300$ K and $V_g = 200$ V, and figure 3 shows electron and hole concentrations, $|\rho_r/e|$ with different gate voltages. As expected, the gate voltages induce electrons and holes in the graphene layer, in which the potential is slightly fluctuated from zero to have nonzero charge densities. Since we have the gates placed far away from the graphene layer, the electron and hole charge densities are smaller than those obtained using the parallel-plate model, $\rho = \rho_s$, and they have sinusoidal-like shapes. Moreover, since we have the ratio of L/d close to

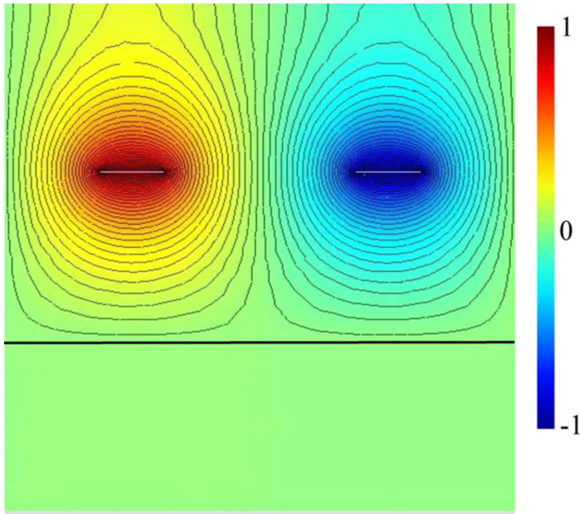

Figure 2. Contour plot for dimensionless potential distribution, φ/V_g, in the structure with $d = 1.5\,\mu$m, $L = 2\,\mu$m, $L_g = 0.5\,\mu$m and $\epsilon = 4$ at $T = 300$ K and $V_g = 200$ V. The bold black line corresponds to the graphene layer, and the grey lines to the gates. In between the graphene layer and the bottom gate there is only an invisible variation of the potential, of the order of 0.1 V.

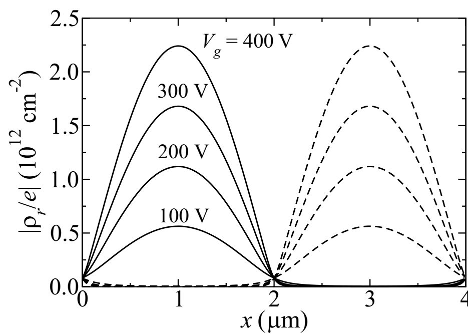

Figure 3. Distributions of electron ($r = e$) and hole ($r = h$) concentrations (solid and dashed lines, respectively), with the same parameters as in figure 2 except gate voltages.

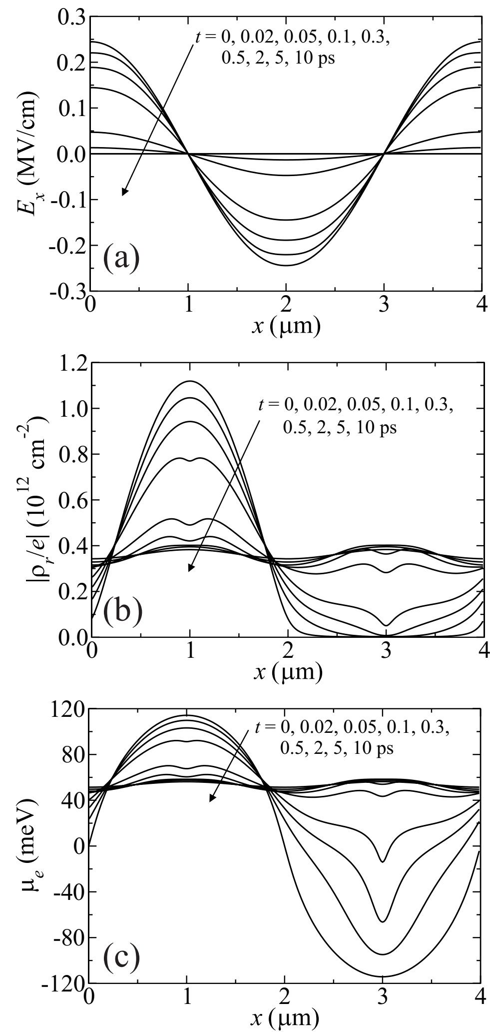

Figure 4. Transient evolution of (a) in-plane electric field, (b) electron concentration and (c) electron quasi-Fermi level with the same parameters as in figure 2 and with $\upsilon_{\rm tot}/\upsilon = 0.5$.

unity, the electric field in the graphene layer created by one gate is cancelled due to the fringe effect by the other gate with opposite-signed voltage, so that the charge densities are further reduced. The electric field is mostly concentrated at the edges of the gates, reflecting that their thickness is much smaller than their length. The maximum field for the highest voltage is close to but still below the breakdown field of SiO_2, $\sim$10 MV cm^{-1} [13]. On the other hand, the field is almost zero in between the graphene layer and the bottom gate due to the screening.

3. Transient lateral drift–diffusion and population inversion

After the abrupt switch-off of the gate voltages, the carriers spread over the graphene layer by the lateral drift–diffusion processes. In the limit of effective intercarrier scattering and momentum relaxation due to the elastic scattering on structural disorders, these processes are governed by the hydrodynamic equations described in the appendix, equations (A.7) and (A.8), coupled with the self-consistent Poisson equation, equation (1). In this section, they were solved numerically as nonlinear equations for the quasi-Fermi levels for electrons and holes, μ_{rxt}, using the standard finite-difference scheme. As mentioned above, we also assume that recombination processes are suppressed.

Figures 4(a)–(c) show the time and position dependences of the electric field, electron concentration, and electron quasi-Fermi level, respectively (see also figure 5). Here the same parameters as in figure 2 were used and we have an additional parameter, $\upsilon_{\rm tot}/\upsilon$, which characterizes the total scattering rate caused by structural disorders (see appendix for details). Hole concentration and its quasi-Fermi level are just equal to mirror images of figures 4(b) and (c). They show two distinct timescales of relaxation of these quantities towards their steady states. One is about 0.5 ps, and it is associated with a process that continues until the electric field created by carriers becomes negligibly small, thus identified as the drift process. The other is longer than 10 ps and is due to the diffusion process. In our case where d is comparable to L and therefore the screening of the inplane electric field by the gates

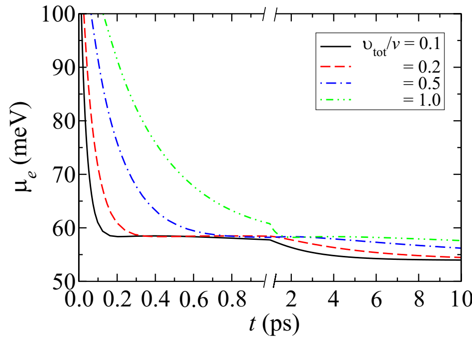

Figure 5. Time dependence of electron quasi-Fermi level at $x = L/2$ with the same parameters as in figure 2 and with different values of υ_{tot}/v.

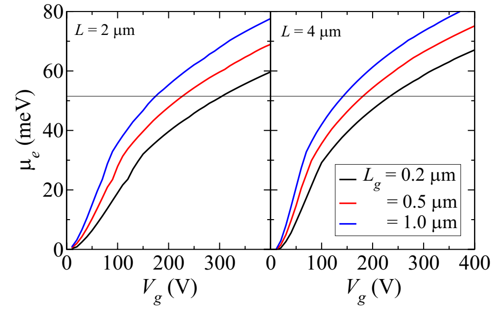

Figure 6. Minimum electron quasi-Fermi level at $t = 0.3$ ps as a function of gate voltage V_g with different half-period lengths L and different gate lengths L_g, together with $\upsilon_{tot}/v = 0.1$. Thin solid lines indicate a half of the photon energy corresponding to $\lambda = 12\,\mu$m.

is ineffective, the timescale of the drift process is always much faster than that of the diffusion process, unless the quasi-Fermi level is not too large. According to [12], in the degenerate case where $\mu_e/k_B T \gg 1$, those characteristic timescales for drift and diffusion processes in the system under consideration can be represented as

$$\tau_{dr} \sim \left(\frac{L}{2v}\right)^2 \nu_{p=\mu_e/v} \frac{\mu_e}{eE_x L}, \quad \tau_D \sim \left(\frac{L}{2v}\right)^2 \nu_{p=\mu_e/v}, \tag{4}$$

where $\nu_p = (\upsilon_{tot}/\hbar)p$ is the scattering rate which depends linearly on the momentum due to the linear density of states. Note that they depend on the quasi-Fermi level (directly, through the self-consistent electric field, and through the collision frequency). With $\mu_e \sim 100$ meV and $E_x \sim 0.2$ MV cm^{-1} taken from figures 4(a) and (c), we have $\tau_{dr} \sim 0.4$ ps. On the other hand, taking into account that the quasi-Fermi level after its stabilization by the drift process is about 50 meV in figure 4(c), we have $\tau_D \sim 40$ ps. These estimations agree well with the timescales mentioned above. It can also be seen from figure 4(c) that more or less uniform distribution of the electron quasi-Fermi level around 50 meV is reached and population inversion in the THz range through the entire graphene layer is established just after the drift process. Qualitatively speaking, this is shorter than the timescale of nonradiative recombination via optical phonons, which is in between 1 and 10 ps (see, for example, [14]).

Figure 5 shows the time dependence of the electron quasi-Fermi level at the centre of the graphene layer with different values of υ_{tot}/v. The timescales increase simultaneously when υ_{tot}/v increases, since the carrier spreading becomes slower when its scattering becomes more frequent. A dimensional analysis shows that the timescales are proportional to υ_{tot}/v. Moreover, they are almost proportional to L^2 when d, L_g and V_g are scaled linearly to L. On the other hand, when fixing d and V_g while scaling L and L_g, the timescale of the drift process is roughly proportional to L, whereas that of the diffusion process remains proportional to L^2.

Figure 6 shows the minimum electron quasi-Fermi level at $t = 0.3$ ps as a function of gate voltage V_g with different half-period lengths L and different gate lengths L_g, together with $\upsilon_{tot}/v = 0.1$. As can be seen in figures 4(c) and 5, we have more or less uniform quasi-Fermi level at the time $t = 0.3$ ps for $\upsilon_{tot}/v = 0.1$, so that it makes sense to discuss about a single quasi-Fermi level (we took the minimum quasi-Fermi level to ensure that population inversion at a certain energy takes place all over the graphene layer). It is clear from figure 6 that the quasi-Fermi level increases monotonically as the voltage increases. Also, it increases as the gate length increases. The condition of population inversion, $\hbar\omega/2 < \mu_r$, for $\lambda = 12\,\mu$m is fulfilled at voltage $V_g > 150$–300 V depending on the gate length L_g and the half-period length L. Since we have neglected the nonradiative recombination, the quasi-Fermi level is solely determined by the initial concentration and, thus, by the electrostatics through the gate voltages and geometrical parameters in a non-trivial way. In particular, threshold voltages for the same value of the quasi-Fermi level are lower for $L = 4\,\mu$m than those for $L = 2\,\mu$m. This lowering is associated with the larger ratio of L/d in the former case, where the cancellation of the electric field in the graphene layer discussed in the previous section is largely relaxed and thereby the induced charge densities as well as the total charges become larger.

From the aspect of the breakdown field, detailed numerical analysis showed that the maximum field at the gate edges to obtain the same value of quasi-Fermi level (say, 60 meV) varies a little by the value of L_g for a fixed value of L, although there exists an optimal value of L_g; for example, for $L = 2\,\mu$m, the maximum field ranges from 2 to 2.4 MV cm^{-1} when $L_g = 0.2$–$1\,\mu$m, having the minimum value at $L_g \simeq 0.4\,\mu$m. In conjunction with the fringing effect mentioned above, the maximum field becomes several times smaller as L changes from $L = 2$ to $4\,\mu$m (reduced to around 0.7 MV cm^{-1}). Note that for too long L, the timescale of the drift process becomes longer, so that the nonradiative recombination effectively takes place before the drift process completes, and the condition of population inversion might not be fulfilled. It is worth mentioning that the results obtained in this section depend only weakly on the temperature through the temperature dependence of the quasi-Fermi level for fixed charge densities. In particular, the quasi-Fermi level becomes slightly larger as the temperature becomes lower. However, this is not the case for gain of the waveguide since values of distribution functions around the quasi-Fermi level mainly determine the gain and depend greatly on the temperature.

4. Transient gain of MSG structures

Finally, we turn to estimate gain in the MSG structure. We determine the electric field of TE mode $E_z \exp(\mathrm{i}kx - \mathrm{i}\omega t)$ propagating along the waveguide from the wave equation

$$\left[\frac{\mathrm{d}^2}{\mathrm{d}z^2} - k^2 + \left(\frac{\sqrt{\varepsilon}\omega}{c}\right)^2\right] E_z = 0. \tag{5}$$

Here we take into account the dielectric loss by introducing the complex dielectric constant, $\varepsilon = \varepsilon' + \mathrm{i}\varepsilon''$, while we assume $\varepsilon' \gg \varepsilon''$. We use the boundary conditions at multi-split and bottom gates $E_{z=\pm d} = 0$. We set to $E_{z=d} = 0$ the boundary condition at the MSGs because the gate period is shorter than the wavelength.

At the graphene layer we use a continuity requirement $E_z|_{z=-0}^{z=+0} = 0$ and a boundary condition

$$\left.\frac{\mathrm{d}E_z}{\mathrm{d}z}\right|_{-0}^{0} = -\mathrm{i}\frac{4\pi\omega}{c^2}\sigma_\omega E_{z=0}, \tag{6}$$

which is written through the high-frequency conductivity of graphene, $\sigma_\omega = \sigma'_\omega + \mathrm{i}\sigma''_\omega$. Using the solution of equations (5) and (6), $E_z \propto \sin\kappa(d - |z|)$ with $\kappa = \sqrt{\varepsilon(\omega/c)^2 - k^2}$, one obtains the dispersion relation between the wavenumber k and the frequency ω:

$$\kappa d \cot(\kappa \mathrm{d}) = 2\pi(-\sigma''_\omega + \mathrm{i}\sigma'_\omega)\frac{\omega d}{c^2}. \tag{7}$$

Neglecting the Drude-like conductivity which is small at the designed mid-IR frequencies of the waveguide (see experimental data in [15] and also discussion at the end of the section) compared with the interband conductivity during the state of population inversion, the conductivity can be written as

$$\sigma'_\omega = \frac{e^2}{4\hbar}\left(1 - \tilde{f}_{exp=p_\omega t} - \tilde{f}_{hxp=p_\omega t}\right), \qquad \sigma''_\omega \simeq 0, \tag{8}$$

where $p_\omega = \hbar\omega/2v$ and $\tilde{f}_r$ is the quasi-Fermi distributions of electrons and holes with temperature T and quasi-Fermi levels μ_r. Here we take the minima of the quasi-Fermi levels to avoid the complication by their position dependence in the transient behaviour discussed in the previous section. In the case of multi-layer graphene, the conductivity roughly becomes m-fold larger, where m is the number of graphene layers.

Taking into account the smallness of σ'_ω/c, we derive the explicit expression of the complex wavenumber from equation (7):

$$kd \simeq \left[\left(\frac{\sqrt{\varepsilon'}\omega d}{c}\right)^2 - \left(\frac{\pi}{2}\right)^2 + \mathrm{i}\frac{\omega d}{c^2}(4\pi\sigma'_\omega + \varepsilon''\omega d)\right]^{1/2}. \tag{9}$$

Away from the condition $\sqrt{\varepsilon'}\omega d/c = \pi/2$, the following approximate expressions for the gain defined as $g_\omega = -\mathrm{Im}\, k$ and the real wavenumber $k_\omega = \mathrm{Re}\, k$ can be obtained from equation (9):

$$g_\omega \mathrm{d} \simeq -\frac{\omega}{2k_\omega c^2}(4\pi\sigma'_\omega + \varepsilon''\omega d),$$
$$k_\omega d \simeq \left[\left(\frac{\sqrt{\varepsilon'}\omega d}{c}\right)^2 - \left(\frac{\pi}{2}\right)^2\right]^{1/2}, \tag{10}$$

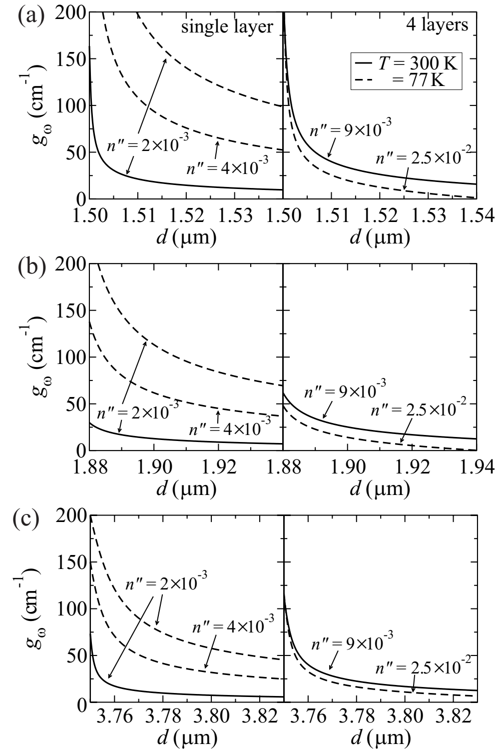

Figure 7. Dependence of gain on the thickness d with operating wavelengths $\lambda = 12$, 15 and 30 μm, quasi-Fermi levels $\mu = 70$, 60 and 40 meV for (*a*), (*b*) and (*c*), respectively, different absorption indices, different temperatures, and different numbers of graphene layers (left panels for single layer and right for four layers).

for $\sqrt{\varepsilon'}\omega d/c > \pi/2$. This case corresponds to a propagating mode with relatively small gain. In the opposite case, we have a quasi-standing-wave mode with high gain, which is not of our interest. Considering the nonnegligible absorption by SiO_2, it turns out that the waveguide under consideration has a rather narrow bandwidth for the propagating mode around the central frequency $\omega = \pi c/2\sqrt{\varepsilon'}d$ when the thickness d is fixed. Writing the imaginary part of the dielectric constant ε'' through the absorption index n'' ($\varepsilon'' \simeq 2\sqrt{\varepsilon'}n''$), the condition of positive gain can be readily obtained from equation (10) for multi-layer graphene:

$$-m\left(1 - \tilde{f}_{exp=p_\omega t} - \tilde{f}_{hxp=p_\omega t}\right) \gtrsim \frac{n''}{\alpha} \simeq \frac{\varepsilon''}{2\sqrt{\varepsilon'}\alpha}, \tag{11}$$

where $\alpha = e^2/\hbar c$ is the fine structure constant. Since the left-hand side in equation (11) is smaller than m, we have a rather universal expression for the maximum allowed value of the dielectric loss for positive gain, $n'' < m\alpha$.

Figure 7 shows the dependence of gain on the thickness d with operating wavelengths $\lambda = 12\,\mu$m, $15\,\mu$m and $30\,\mu$m, quasi-Fermi levels $\mu = 70$ meV, 60 meV and 40 meV, respectively, different absorption indices, different temperatures, and different numbers of graphene layers, using equation (9). Note that for each wavelength under consideration the condition of population inversion is satisfied with corresponding quasi-Fermi level. We plotted figure 7 for the thickness larger than $d_0 = \pi c/2\sqrt{\varepsilon'}\omega$ ($d_0 = 1.5\,\mu$m, $1.88\,\mu$m and $3.75\,\mu$m for $\lambda = 12\,\mu$m, $15\,\mu$m and $30\,\mu$m,

respectively), which correspond to the propagating mode. At the condition $d = d_0$, the values of the gain and real wavenumber coincide. For $d < d_0$, the mode transits abruptly to a quasi-standing-wave mode, which has a real wavenumber in the propagation direction much smaller than d_0. It is seen from figure 7 that the gain above 100–200 cm^{-1} is achieved and that the gain decreases as the thickness increases, whereas the real wavenumber increases. These dependences can be understood from the fact that the propagating mode can be considered roughly as the superposition of electromagnetic waves with wavevectors $(k_\omega, \pm k_d)$, where $k_d = \pi/2d$ is the wavenumber in the z-direction. These electromagnetic waves propagate with reflection by the multi-split and bottom gates and with passage through the gain region, i.e., the graphene layer. With increasing d, the electromagnetic waves are more inclined to the propagation direction in order to match the absolute value of their wavevectors to $\sqrt{\epsilon'}\omega/c = 2\pi/\lambda$, so that the real wavenumber k_ω along the propagation direction increases; the matching condition is just given by equation (10). In turn, this increase in the real wavenumber accompanies the rapid gain decrease near $d = d_0$, as it reduces 'the number of passages' of the electromagnetic waves through the gain region in unit length along the propagation direction. Taking these dependences into account, one needs to choose carefully a proper value of the thickness d (slightly larger than d_0) to have sufficiently large real wavenumber while keeping the gain larger than losses. Conversely, once the thickness is determined, the operating wavelength is limited in a rather narrow-band range.

Figure 8 shows the dependence of gain on the quasi-Fermi level with a fixed thickness for each operating wavelength. The real wavenumber does not noticeably change by the quasi-Fermi level. It is seen in figure 8 that the gain increases almost linearly to the quasi-Fermi level, starting from the onset of positive gain described by equation (11), and it saturates after the increase in the quasi-Fermi level by temperature. Owing to the factor $1/d$ in the expression of k, the gain increases as the operating wavelength decreases.

Figures 7 and 8 exhibit a relatively strong temperature-dependence of the gain. This reflects the fact that the interband negative conductivity is linearly dependent on values of distribution functions as seen in equation (8), resulting in the increase in its absolute value for the frequency below the quasi-Fermi level as the temperature decreases. Thus, at low temperature the positive gain appears for the higher absorption index. It in turn means that for a fixed absorption index the threshold quasi-Fermi level for the positive gain becomes lower at lower temperature, although above the threshold the positive gain quickly saturates and the magnitude remains more or less the same below $T = 77$ K. Also, the introduction of multi-layer graphene greatly enhances the gain. The absorption index n'' experimentally measured for fused silica glasses in [11] is above 10^{-2}, although a smaller value is expected by a thermally grown crystalline SiO_2 on a Si substrate. As seen in the right panels of figure 7, the dielectric loss in such a case can be overcome by introducing multi-layer graphene and by operating at low temperature. One can alternatively use nonpolar materials with no large absorption in the mid-IR wavelength as a part of the MSG structure, e.g., in the substrate region, where materials with relatively low breakdown field are permissible.

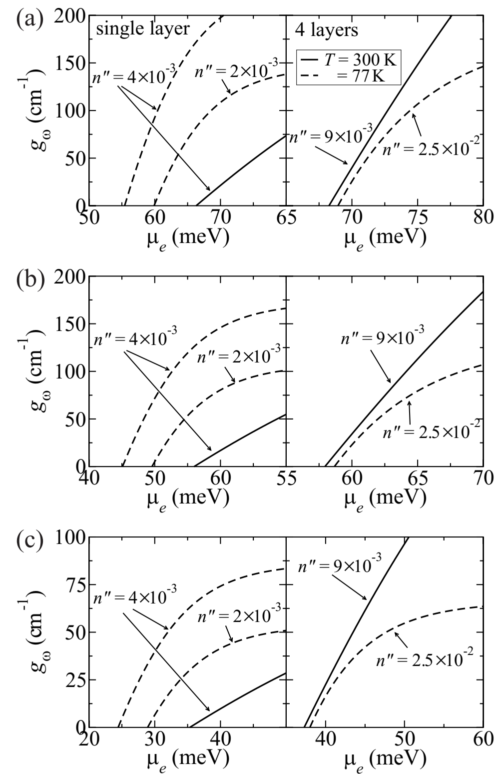

Figure 8. Dependence of gain on the quasi-Fermi level with fixed thickness d ($\lambda = 12\,\mu$m, 15 μm, 30 μm and $d = 1.51\,\mu$m, 1.89 μm, 3.78 μm for (a), (b), (c), respectively). Other parameters are the same as in figure 7.

It was checked that the Drude-like conductivity, with increased electron and hole concentrations during the state of population inversion and with the scattering rate by disorders ($\upsilon_{tot}/v > 0.1$), becomes influential when the wavelength is longer than 30 μm. In particular, it decreases the values of the gain in figure 7 and increases the threshold of the gain in figure 8. Also, it is anticipated that the imaginary part of the Drude-like conductivity changes the condition of the propagating mode, $d > d_0$, due to reflection of electromagnetic waves at the graphene layer. However, these effects are not essential for physics discussed in this section, although they add more complication to the design of the MSG structure, which is beyond the scope of this paper.

5. Conclusions

With the main goal to find conditions for an effective stimulated emission regime without the optical-phonon emission, we have examined a new pumping scheme for a graphene layer modulated by spatio-temporally varied voltages which are applied through the multi-split top gates. We found that a transient lasing regime in the mid-IR spectral region is realized in the MSG structure with micrometer width and period. Gain above hundred(s) cm^{-1} for operating wavelengths $\lambda = 12$, 15

and 30 μm was obtained if the gate voltage is around 100–300 V. This is comparable to gain in typical quantum cascade lasers [16] and the transient stimulated emission takes place if waveguide losses are comparable to losses in quantum cascade lasers.

Let us discuss the assumptions we used in the presented calculations. Because of a lack of data on graphene structures with multi-split gates, the above consideration was separated into description of the different stages of evolution (i.e., diffusion from the separated electron and hole distributions at initial moment to the homogeneous electron–hole plasma) and estimates of the gain at a time when the recombination caused by optical phonons and Auger processes is negligible (see numerical data for recombination rate in [17]). The inclusion of the Auger processes, which are forbidden by the vanishing phase space for transition for the case of strictly linear band dispersion [18], requires special theoretical investigation to account not only for the energy-level broadening [19] but also band renormalization due to electron–electron and/or electron–disorder interaction, and it is beyond the scope of this paper. We considered the simplified periodical geometry (the edge effects require a special consideration) placed into a media with homogeneous dielectric constant. A more complicate spatio-temporal simulation does not change the numerical estimates presented here and it should be performed for a specific structure. In calculating the waveguide mode of the MSG structures we assumed the zero field at the plane where the multi-split gate is placed. Other assumptions are rather standard. We used the semi-phenomenological model of elastic scattering under description of the diffusion process in the appendix, assuming the rate of long-range disorder scattering is proportional to carrier momentum (see discussion and conditions in [20]), and restricted ourselves by the single-particle approach. For the mid-IR region, one can omit the intraband (Drude-like) conductivity in realistic graphene samples; see experimental data and discussion in [15]. In addition, we do not consider a nonlinear regime of lasing, which is essential under high concentrations (limited by $V_{\rm g}$) or for long times, so that a pulse duration is not determined here. An estimate of the recovery time requires a special consideration.

To conclude, we believe that the results obtained open a way for a further experimental investigation of the transient stimulated emission in the mid-IR spectral region and that the use of the MSG structures suggested can open a new possibility for mid-IR application. Note that attempts for realization of the graphene-based laser in the THz and near-IR spectral region were performed in recent years [5–9]. Similar investigations in the mid-IR spectral region should be useful for realization of devices in that region.

Acknowledgments

This work was supported by JSPS Grant-in-Aid for Specially Promoted Research (#23000008), by JSPS Grant-in-Aid for Young Scientists (B) (#23760300), and by NSF TERANO award 0968405. Also, FTV and VVM are grateful to RIEC as the major amount of this work was done during their visit to Tohoku University on invitation of RIEC.

Appendix. Hydrodynamic approach

The electron and hole contributions ($r = e$ and h) to the charge and current densities, ρ_{rxt} and $\boldsymbol{I}_{rxt}$, are determined by the standard quasi-classical relations:

$$\left|\begin{matrix}\rho_{rxt}\\ \boldsymbol{I}_{rxt}\end{matrix}\right| = 4s_r e \int \frac{{\rm d}\boldsymbol{p}}{(2\pi\hbar)^2} \left|\begin{matrix}1\\ \boldsymbol{v}_p\end{matrix}\right| f_{rxpt}, \qquad (A.1)$$

where f_{rxpt} stands for electron or hole distributions and $s_{\rm e} = -1$ and $s_{\rm h} = +1$. The spatio-temporal evolution of the quantities (A.1) is governed by the quasi-classical kinetic equation for f_{rxpt}, see [21]. In this paper, we consider the case of effective momentum relaxation due to the elastic scattering on structural disorders, under the conditions $\nu_m \equiv \nu_{\bar{p}} \gg |e\boldsymbol{E}|/\bar{p}$ (here $\bar{p}$ is a characteristic momentum) and $\nu_m \gg v/L$, when the distribution is given by $f_{rxpt} = f_{rxpt} + \Delta f_{rxpt}$ with a weak anisotropic part, $\Delta f_{rxpt} = -\Delta f_{rx,-pt}$. The linearized equation for Δf gives the anisotropic distribution in the form:

$$\Delta f_{rxpt} = -\left(\boldsymbol{v_p}\cdot\boldsymbol{\nabla}_x + s_r e\boldsymbol{E}_{xt}\cdot\boldsymbol{\nabla}_p\right) f_{rxpt}/\nu_p, \qquad (A.2)$$

where we used the elastic collision integral $-\nu_p \Delta f_{rxpt}$ written through the momentum relaxation frequency ν_p. The isotropic part of distribution f_{rxpt} is governed by the equation:

$$\frac{\partial f_{rxpt}}{\partial t} + \Phi_{rxpt} = \sum_k J_k(f_{xt}|rp), \qquad (A.3)$$

$$\Phi_{rxpt} = \overline{\left(\boldsymbol{v_p}\cdot\boldsymbol{\nabla}_x + s_r e\boldsymbol{E}_{xt}\cdot\boldsymbol{\nabla}_p\right)\Delta f_{rxpt}},$$

where overline means the averaging over $\boldsymbol{p}$-plane angle and summation over k includes the non-elastic scattering mechanisms ($k = ac, opt, cc$ for relaxation via acoustic and optical phonons or carrier-carrier scattering).

A general solution for equations (A.2) and (A.3) is determined both by external field and by relative contributions of the nonelastic scattering mechanisms. Below we consider the case of an effective intercarrier scattering, under the condition

$$\nu_m \gg \nu_{cc} \gg \nu_{ac}, \qquad \nu_{opt}, \qquad (A.4)$$

where ν_k means the scattering rate for kth channel. The solution is given by the quasiequilibrium distribution:

$$\widetilde{f}_{rxpt} = \{\exp[(vp - \mu_{rxt})/T_{xt}] + 1\}^{-1} \qquad (A.5)$$

written without a negligible correction of the order of $(\nu_{ac}, \ \nu_{opt})/\nu_{cc}$. Note that $J_{cc}(\widetilde{f}_{xt}|rp) = 0$ and the main term of equation (A.3) vanishes by the solution (A.5) with any effective quasi-Fermi levels, μ_{rxt}, and an arbitrary effective temperature, T_{xt}.

In order to obtain μ_{rxt} and T_{xt}, we take into account that

$$\frac{4}{L^2}\sum_{\boldsymbol{p}} \left|\begin{matrix}1\\ vp\end{matrix}\right| J_{cc}\left(f_{xt}|r\boldsymbol{p}\right) = 0, \qquad (A.6)$$

i.e., the intercarrier scattering does not change the electron and hole concentrations and the energy of carriers, as it follows from the explicit expression for J_{cc}. Thus, the functions μ_{rxt} and T_{xt} are determined from the balance equations for the charge and energy densities, while $\boldsymbol{I}_{rxt}$ is determined

through μ_{rxt} and T_{xt} according to equations (A.1), (A.2) and (A.5). Integrating equation (A.3) over $\boldsymbol{p}$-plane, one obtains the balance equations for electron and hole charge densities:

$$\frac{\partial \rho_{rxt}}{\partial t} + \nabla_x \cdot \mathbf{I}_{rxt} = \left(\frac{\partial \rho_{rxt}}{\partial t}\right)_{\mathrm{rec}}, \qquad \text{(A.7)}$$

where we take into account that $4e\int d\boldsymbol{p}\Phi_{rxpt}/(2\pi\hbar)^2 = s_r\nabla_x \cdot \boldsymbol{I}_{rxt}$ and the right-hand side describes the recombination processes[4]. We consider the momentum relaxation caused by Gaussian and short-range disorder potentials, [20] with the total rate ν_p. The Gaussian disorder is described by the correlation function $\overline{V}^2\exp[-(\boldsymbol{x}-\boldsymbol{x}')^2/2l_c^2]$, where $\overline{V}$ is the averaged energy and l_c is the correlation length. Within the Born approximation, the correspondent relaxation rate reads $\nu_p = (\upsilon_d p/\hbar)\Psi(pl_c/\hbar)(1+\upsilon_0/\upsilon_d)$ where we have introduced the dimensionless function $\Psi(z) = \mathrm{e}^{-z^2}I_1(z^2)/z^2$ with the first-order Bessel function of an imaginary argument, $I_1(z)$ and the characteristic velocity $\upsilon_d = \pi(\overline{V}l_c/\hbar)^2/(2\upsilon)$. The relaxation rate due to the short-range disorder potential has a similar (if $l_c \to 0$) dependence $\propto \upsilon_0 p/\hbar$, with an explicit expression for the characteristic velocity υ_0 given in reference [20]. Assuming that the carrier temperatures are equal to the lattice temperature, $T_{xt} = T$, the current density can be written in the following expression:

$$\boldsymbol{I}_{rxt} = \sigma_{rxt}\left(\boldsymbol{E}_{rxt} - \frac{s_r}{e}\nabla_x\mu_{rxt}\right), \qquad \text{(A.8)}$$

where the local conductivity σ_{rxt} is given by $\sigma_{rxt} \simeq (e^2\upsilon/\pi\hbar\upsilon_{\mathrm{tot}})\widetilde{f}_{rxp=0t}$. We assumed here that the total scattering rate is proportional to the momentum, i.e., $\nu_p = (\upsilon_{\mathrm{tot}}/\hbar)p$ with the characteristic velocity $\upsilon_{\mathrm{tot}} = \upsilon_0 + \upsilon_d$ of the total scattering rate. The value of υ_{tot} can be estimated as $\upsilon_{\mathrm{tot}}/\upsilon = 6.58\times10^{-2} - 10^{-1}$, which correspond to the value of the total scattering rate 10^{13}–10^{14} s^{-1} at $\upsilon p = 100$ meV.

References

[1] Koechner W 2003 *Solid-State Laser Engineering* (New York: Springer)
Silfvast W T 2003 *Laser Fundamentals* (New York: Cambridge University Press)

[2] Gmachl C, Capasso F, Sivco D L and Cho A Y 2001 *Rep. Prog. Phys.* **64** 1533

[3] Komiyama S 1982 *Adv. Phys.* **31** 255

[4] Castro Neto A H, Guinea F, Peres N M R, Novoselov K S and Geim A K 2009 *Rev. Mod. Phys.* **81** 109
Novoselov K S 2011 *Rev. Mod. Phys.* **81** 837

[5] Ryzhii V, Ryzhii M and Otsuji T 2007 *J. Appl. Phys.* **101** 083114

[6] Vasko F T 2010 *Phys. Rev.* B **82** 245422
Satou A, Otsuji T and Ryzhii V 2011 *Japan J. Appl. Phys.* **50** 070116

[7] Boubanga-Tombet S, Chan S, Watanabe T, Satou A, Ryzhii V and Otsuji T 2012 *Phys. Rev.* B **85** 035443

[8] Prechtel L, Song L, Schuh D, Ajayan P, Wegscheider W and Holleitner A W 2012 *Nature Commun.* **3** 646

[9] Li T, Luo L, Hupalo M, Zhang J, Tringides M C, Schmalian J and Wang J 2012 *Phys. Rev. Lett.* **108** 167401

[10] Popov V V, Fateev D V, Otsuji T, Meziani Y M, Coquillat D and Knap W 2011 *Appl. Phys. Lett.* **99** 243504
Watanabe T *et al* 2012 *Solid-State Electron.* **78** 109

[11] Kitamura R, Pilon L and Jonasz M 2007 *Appl. Opt.* **46** 8118

[12] Vasko F T and Mitin V V 2012 *Appl. Phys. Lett.* **101** 151115

[13] Sze S M and Ng K K 2007 *Physics of Semiconductor Devices* (Hoboken, NJ: Wiley-interscience)

[14] Satou A, Ryzhii V, Kurita Y and Otsuji T 2013 *J. Appl. Phys.* **113** 143108

[15] Horng J *et al* 2011 *Phys. Rev.* B **83** 165113
Ren L *et al* 2012 *Nano Lett.* **12** 3711
Vasko F T, Mitin V V, Ryzhii V and Otsuji T 2012 *Phys. Rev.* B **86** 235424

[16] Jovanović V D, Indjin D, Ikonić Z and Harrison P 2004 *Appl. Phys. Lett.* **84** 2995
Yao Y, Charles W O, Tsai T, Chen J, Wysocki G and Gmachl C F 2010 *Appl. Phys. Lett.* **96** 211106
Mujagić E, Schwarzer C, Yao Y, Chen J, Gmachl C and Strasser G 2011 *Appl. Phys. Lett.* **98** 141101

[17] Rana F, George P A, Strait J H, Dawlaty J, Shivaraman S, Chandrashekhar Mvs and Spencer M G 2009 *Phys. Rev.* B **79** 115447
Rana F, Strait J H, Wang H and Manolatou C 2010 arXiv:1009.2626
Ryzhii V, Ryzhii M, Mitin V, Satou A and Otsuji T 2011 *Japan J. Appl. Phys.* **50** 094001

[18] Foster M S and Aleiner I L 2009 *Phys. Rev.* B **79** 085415

[19] Malic E, Winzer T, Bobkin E and Knorr A 2011 *Phys. Rev.* B **84** 205406

[20] Vasko F T and Ryzhii V 2007 *Phys. Rev.* B **76** 233404
Romanets P N and Vasko F T 2011 *Phys. Rev.* B **83** 205427

[21] Vasko F T and Raichev O E 2005 *Quantum Kinetic Theory and Applications* (New York: Springer)

[4] The sheet charge and the total current densities, $Q_{xt} = \sum_{r=e,h}\rho_{rxt}$ and $\boldsymbol{I}_{xt} = \sum_{r=e,h}\boldsymbol{I}_{rxt}$, are connected by the continuity equation: $(\partial Q_{xt}/\partial t) + \mathrm{div}\boldsymbol{I}_{xt} = 0$. Note, that a total number of electrons (or holes) are not conserved due to generation-recombination processes in the gapless material.